Electronic Supplementary Material (ESI) for Reaction Chemistry & Engineering.

Supplementary Information

Light as Reaction Parameter – Systematic Wavelength Screening in Photochemical Synthesis

Christian P. Haas,[†a] Thomas Roider,[†a] Reinhard W. Hoffmann[a] and Ulrich Tallarek*[a]

Department of Chemistry, Philipps-Universität Marburg, Hans-Meerwein-Strasse 4, 35032 Marburg, Germany. E-mail: tallarek@staff.uni-marburg.de; Web: http://www.uni-marburg.de/fb15/ag-tallarek.

[†] Both authors contributed equally to this work.

S1) General experimental information....3

S2) Two-dimensional reaction–analysis setup....4

S3) Photoreactor design....11

S4) Irradiance-matching of the LED arrays....16

S5) Reaction time screening....23

S6) Offline NMR analysis....24

S1) General experimental information

All chemicals were received from Sigma–Aldrich (St. Louis, MO) in a purity of at least 98% and were used without further purification. Eosin Y was offered only with a purity of >75% and was bought in its acidic form (CAS number 15086-94-9). Acetonitrile (HiPerSolv CHROMANORM for HPLC) was purchased from VWR Chemicals (Darmstadt, Germany) and water was obtained from a Milli–Q gradient purification system (Millipore, Bedford, MA). The ^{1}H NMR (500 MHz) and ^{13}C NMR (125 MHz) spectra were recorded at ambient temperature on a Bruker Avance 500 NMR spectrometer. ^{19}F NMR spectra (282 MHz) were recorded on a Bruker Avance 300 NMR spectrometer. The chemical shifts are reported in parts per million (ppm) relative to the solvents DMSO-d_6 (^{1}H NMR 2.50 ppm; ^{13}C NMR 39.52 ppm) and $PhCF_3$ (^{19}F NMR −63.2 ppm). Multiplicities are reported using the following abbreviations: s (singlet), d (doublet), t (triplet), m (multiplet).

S2) Two-dimensional reaction–analysis setup

The two-dimensional flow platform, described in detail previously,[S1] was adapted to the test reaction between 2-methylindole (**1**) and nonafluoro-1-iodobutane (**2**) such that the two substrates (**1**, **2**) as well as the amine base 1,8-diazabicyclo[5.4.0]undec-7-ene (DBU) and the photoredox catalyst eosin Y could be mixed independently with acetonitrile. The pump assembly was composed of two HPLC pumps providing five independent channels to precisely control the flow rate on the photoreactor and the starting concentrations of each reactant. Between pumps and photoreactor a back-pressure regulator (adjusted to 50 bar) was placed to ensure noise-free operation of the HPLC pumps. On the reactor, no back-pressure was applied. Behind the reactor, a 2-position/6-port valve with an injection loop was mounted, which transferred an injection volume of 1.3 µL to an online coupled HPLC system. An inline diode array detector (DAD) was used to verify when the reactor was operating in steady-state. All parts of the system could be programmed depending on the experiment time so that parameter adjustments as well as sampling for the HPLC proceeded fully automated. Scheme S1 illustrates the flow path of the setup.

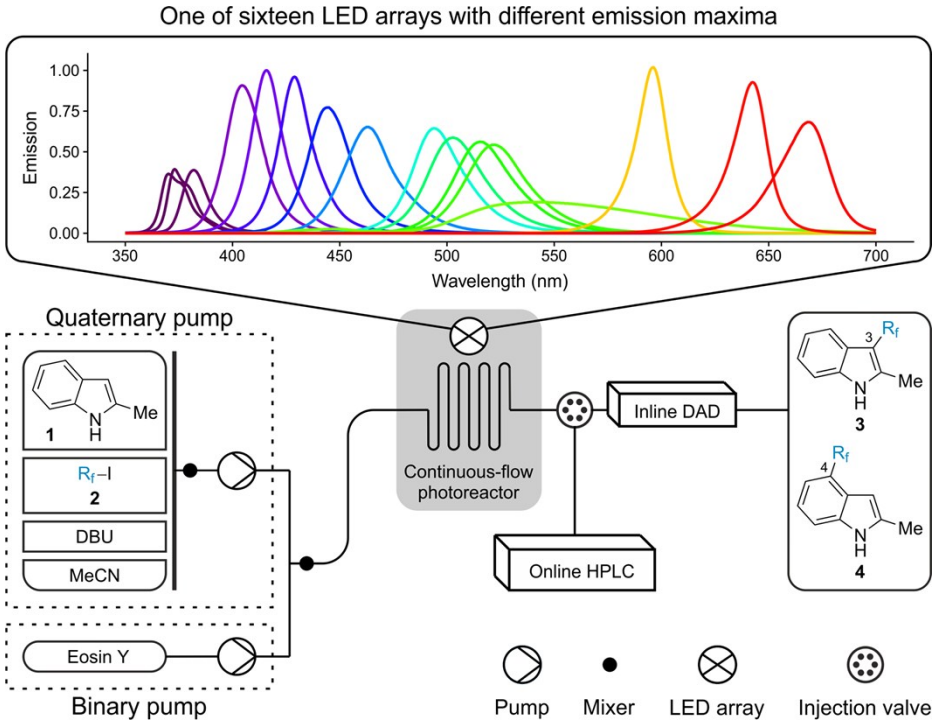

Scheme S1. Flow path of the employed setup and the 16 different irradiance-matched emission spectra of the LED arrays used for the systematic wavelength screenings. R_f–I labels according to the main text the perfluoroalkylated butyl iodide **2**.

A photograph of the employed system (without photoreactor) is shown in Figure S1. All incorporated hardware components have been received from Agilent Technologies (Santa Clara, CA).

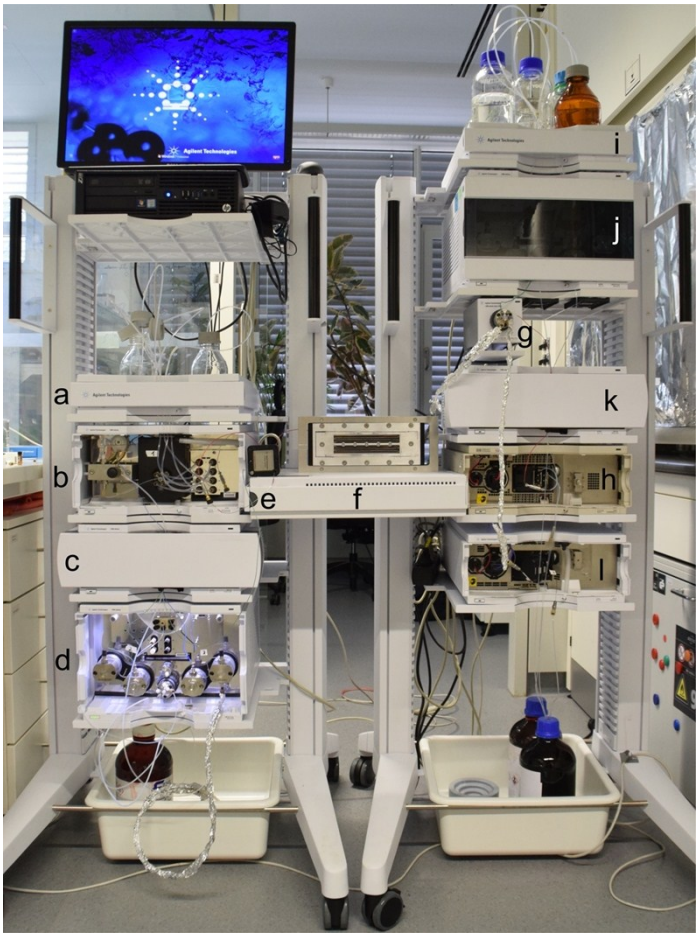

Figure S1. Reaction: a) Substrate solutions; b) quaternary pump (Agilent 1260 Infinity Series, G1311B); c) thermostatted HPLC column compartment (Agilent 1290 Infinity Series, G1316C); d) binary pump (Agilent 1290 Infinity Series, G4220A); e) Jet Weaver V35 Mixer; f) photoreactor; g) 2-position/6-port valve (Agilent 1290er Series, G1170A); h) inline DAD (Agilent 1200 Series, G1315C). HPLC analysis: i) Eluents; j) binary pump (Agilent 1290 Infinity Series, G4220A); k) thermostatted HPLC column compartment (Agilent 1290 Infinity Series, G1316C) with separation column; l) DAD (Agilent 1290 Infinity Series, G4212A).

The chromatographic separation process of the online coupled analytical HPLC system was optimized such that all reactants, additives, products, and side products were baseline-separated in the shortest possible analysis time. Therefore, the separation was performed at 25 °C on a monolithic separation column (C18 Chromolith High Resolution; RP 18-e, 100–4.6 mm) from Merck KGaA (Darmstadt, Germany) with water and acetonitrile (+ 0.1% trifluoroacetic acid) as eluents. Table S1

summarizes the gradient developed for the specific separation problem, resulting in analytical cycles of 14 minutes.

Table S1. Gradient developed for the online coupled HPLC system. The flow rate remained constant at 2 mL min^{-1}.

Time (min)	Water (%)	Acetonitrile (%)
0.00*	80	20
5.00	55	45
7.00	40	60
10.00	40	60
10.90	0	100
12.40	0	100
12.41	80	20
14.00*	80	20

*Injection

However, the separation of the regioisomeric products **3** and **4** remained a challenge, since they persistently coeluted on C18 reversed-phase columns (see further below for more details). A typical chromatogram is shown in Figure S2 with the signals of interest assigned.

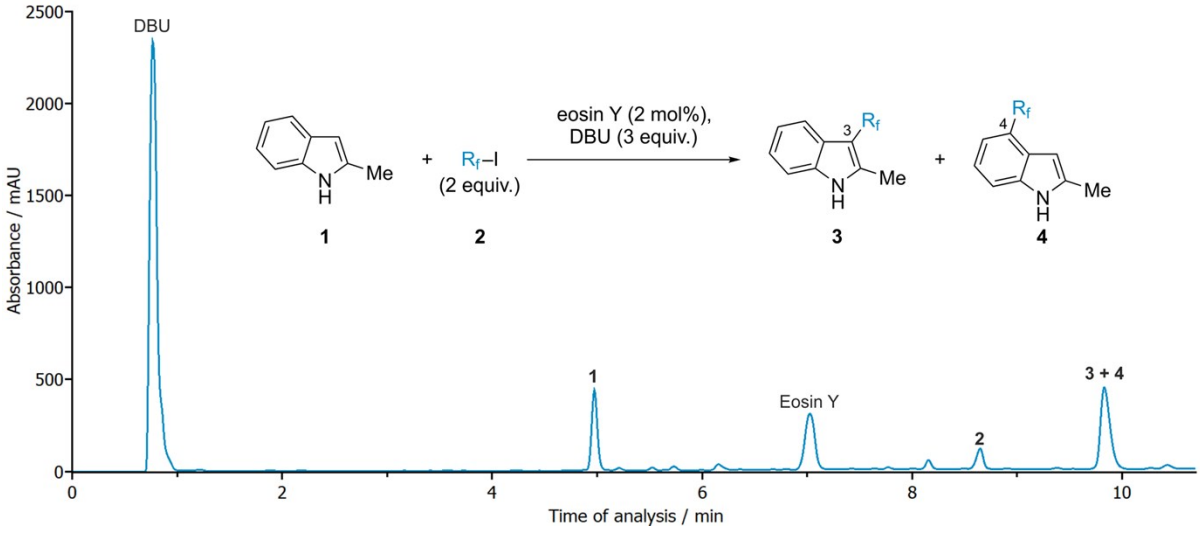

Figure S2. Typical chromatogram obtained at the detection wavelength of 243 nm.

To use the online coupled HPLC system for quantification, it was programmed to calibrate itself fully automized for the two substrates and the product. Therefore, a solution with a known concentration of the respective substrate or product was placed in the first dimension and the system was programmed to mix it in different volumetric ratios with acetonitrile. Programmed switches of the injection valve delivered concentration-dependent HPLC signals in the second dimension using the gradient described in Table S1. The calibration curves of the substrates 2-methylindole (**1**) and nonafluoro-1-iodobutane (**2**) showed linear behavior in the calibrated range (illustrated in Figures S3 and S4). These calibration curves also confirm the precision and the high reproducibility of the system, since all ten single-point analyses for each calibration laid almost perfectly on a straight line.

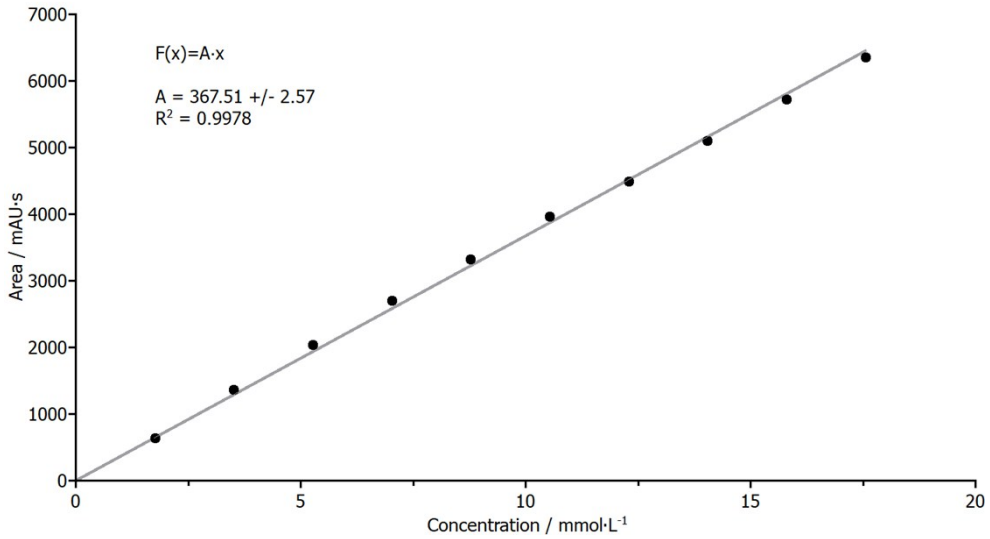

Figure S3. Calibration curve of the substrate 2-methylindole (**1**) at the detection wavelength of 243 nm.

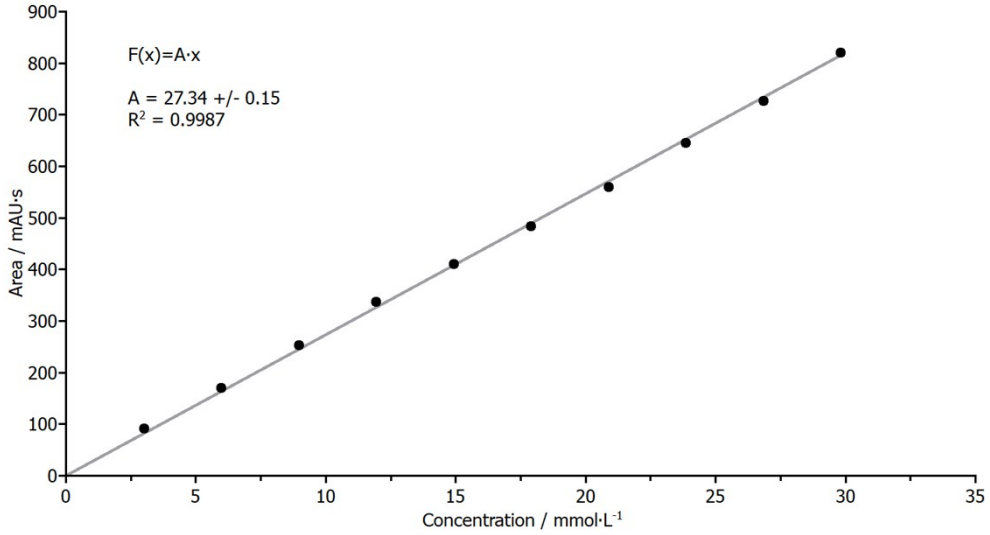

Figure S4. Calibration curve of the substrate nonafluoro-1-iodobutane (**2**) at the detection wavelength of 260 nm.

Since the regioisomeric products **3** and **4** were not separated in the chromatographic process, a new concept for their quantification was used based on the significantly different UV-Vis absorption spectra shown in Figure S5.

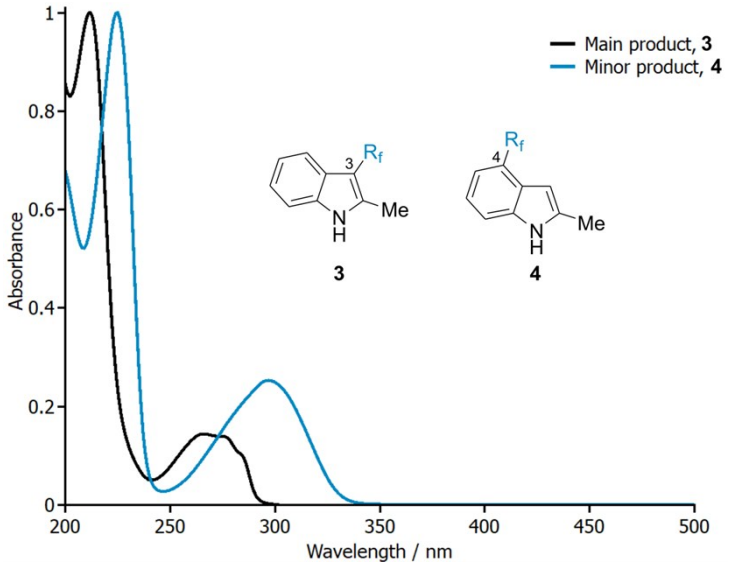

Figure S5. UV-Vis spectra of the regioisomeric perfluorobutylated indoles **3** and **4**.

Quantification is based on the bathochromic shift of the 4-perfluorobutylated indole **4** compared to its regioisomer **3**. Differently composed mixtures of **3** and **4** were calibrated at two different wavelengths, 243 nm and 322 nm. At 322 nm the regioisomer **4** was calibrated in the same manner as the substrates **1** and **2**, since the

regioisomer **3** did not show any absorbance at this detection wavelength. The resulting calibration curve is shown in Figure S6.

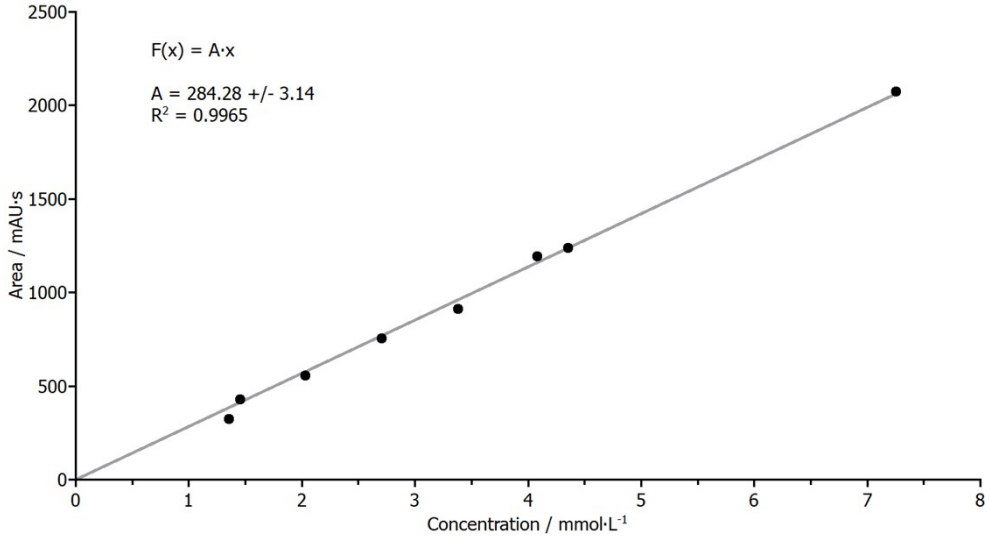

Figure S6. Calibration curve of the 4-perfluorobutylated indole **4** at a detection wavelength of 322 nm.

The calibration at 243 nm (where both regioisomers absorb light) was performed for different molar ratios of **3** and **4**. The fraction of the HPLC signal belonging to the absorbance of regioisomer **3** could be calculated via equations using the defined different molar ratios. The resulting calibration curve of the 3-perfluorobutylated indole **3** is shown in Figure S7.

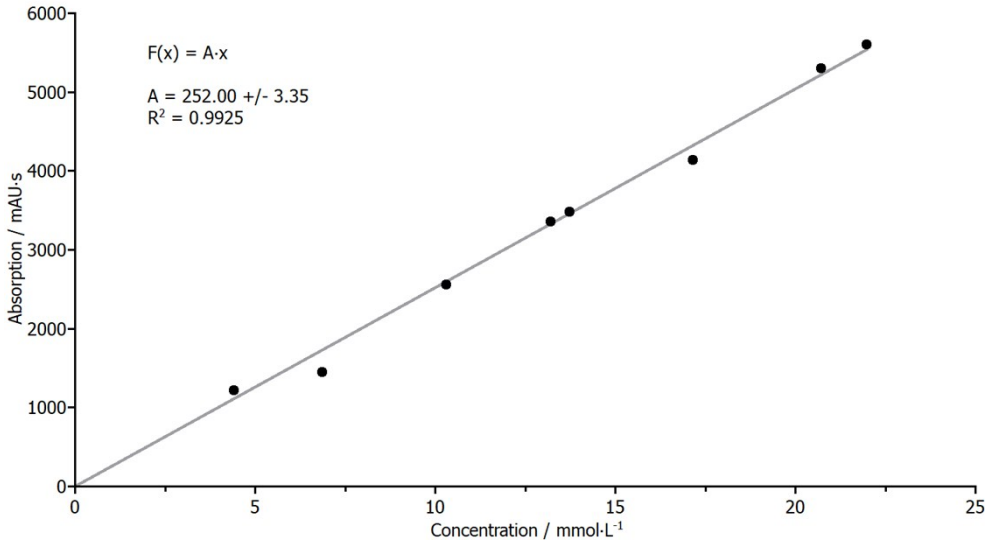

Figure S7. Calibration curve of the 3-perfluorobutylated indole **3** at a detection wavelength of 243 nm.

This calibration allowed to determine unknown concentrations of the regioisomers **3** and **4** via HPLC analysis only by detecting at two different wavelengths (i.e., at 322 nm to determine the concentration of **4** and at 243 nm to determine the concentration of **3** with the concentration of **4** already known), even though the regioisomers could not be separated with the HPLC column.

S3) Photoreactor design

To enable the matching procedure with a spectroradiometer (not possible in tubing photoreactors), a planar photoreactor was designed in-house with geometrically aligned LED array housings. Figure S8 illustrates the modular setup of the reactor. The plates (b–e), which are screwed together, have dimensions of 230 mm length and 90 mm width and thicknesses as given in Figure S8. The reactor window was made of aluminium to provide mechanical stability and confine the irradiated area of the reactor to dimensions of 140 mm length and 40 mm width, with a brace in the middle for added stability. The LED array housing was aligned such that it was seated on the window edges and all LEDs were inside the notched area.

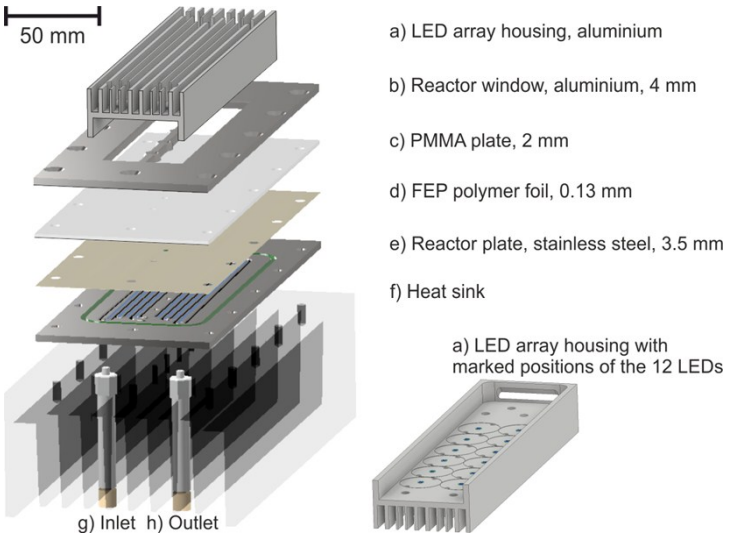

Figure S8. Modularly designed flow photoreactor: a) LED array housing made of aluminium with an integrated heat sink on the rear side; b) reactor window for confinement of the irradiated area and mechanical stability; c) polymethylmethacrylate (PMMA) plate for mechanical stability of the pane; d) fluorinated ethylene propylene (FEP) polymer foil providing chemical resistance against organic solvents; e) stainless steel reactor plate; f) heat sink; g) reactor inlet; h) reactor outlet.

To guarantee highest possible transmission of the window pane combined with a high mechanical stability as well as high chemical resistance, a combination of a thicker polymethylmethacrylate (PMMA) plate and a thinner fluorinated ethylene propylene (FEP) polymer foil (KELUX Kunststoffe GmbH, Geldern, Germany) was assembled. This unique setup delivered a high mechanical stability (PMMA plate) combined with chemical resistance against organic solvents (FEP foil). The transmission of this polymer pane was ~80% for wavelengths >400 nm due to the careful adjustment of the thicknesses of the polymer layers. For wavelengths <400 nm the transmission of the pane dropped significantly, as shown in Figure S9.

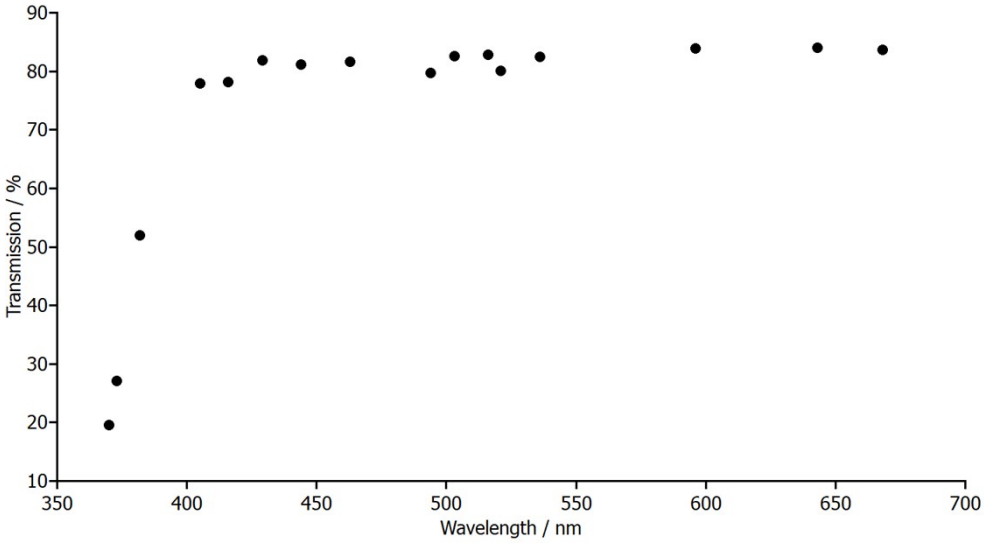

Figure S9. Transmission profile of the polymer layers (2 mm PMMA and 0.13 mm FEP) used as window pane under irradiation of the 16 employed LED arrays.

The heat sink (0.5 K W^{-1}, ABL Components, Birmingham, UK) was fixed on the rear side of the reactor with a heat conduction foil (SFT80-0.15, 0.2 K W^{-1}, AMEC Thermasol, Norfolk, UK) placed between reactor plate and heat sink. With this setup, the highest measured temperature increase directly behind the photoreactor was ~1 °C using the 405nm-array at maximum current (700 mA). Inlet and outlet of the reactor were equipped with standardized threads to make them compatible with HPLC tubings and fittings. Photographs of the final setup are shown in Figure S10 with the LED array placed on top of the photoflow reactor.

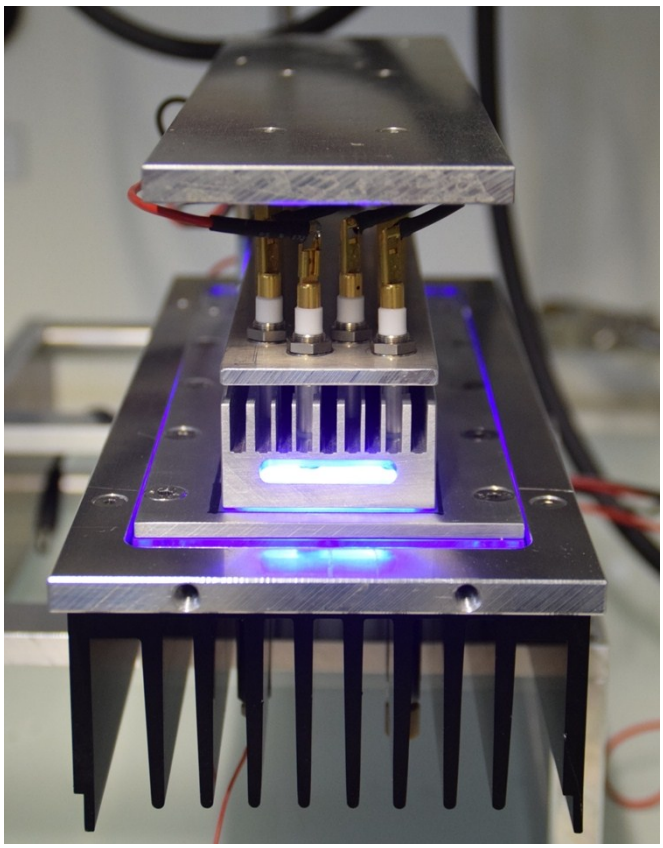

Figure S10. Photograph of the reactor setup ready-to-go.

The centerpiece of this setup was the reactor plate, into which a channel (1.5 mm width and 0.5 mm depth) was milled covering the whole reactor window. Sealing (fluoroelastomer FPM) was purchased from Arcus (Seevetal, Germany) and fixed also between reaction channels to prevent shortcutting between them. A technical drawing with relevant dimensions is given in Figure S11.

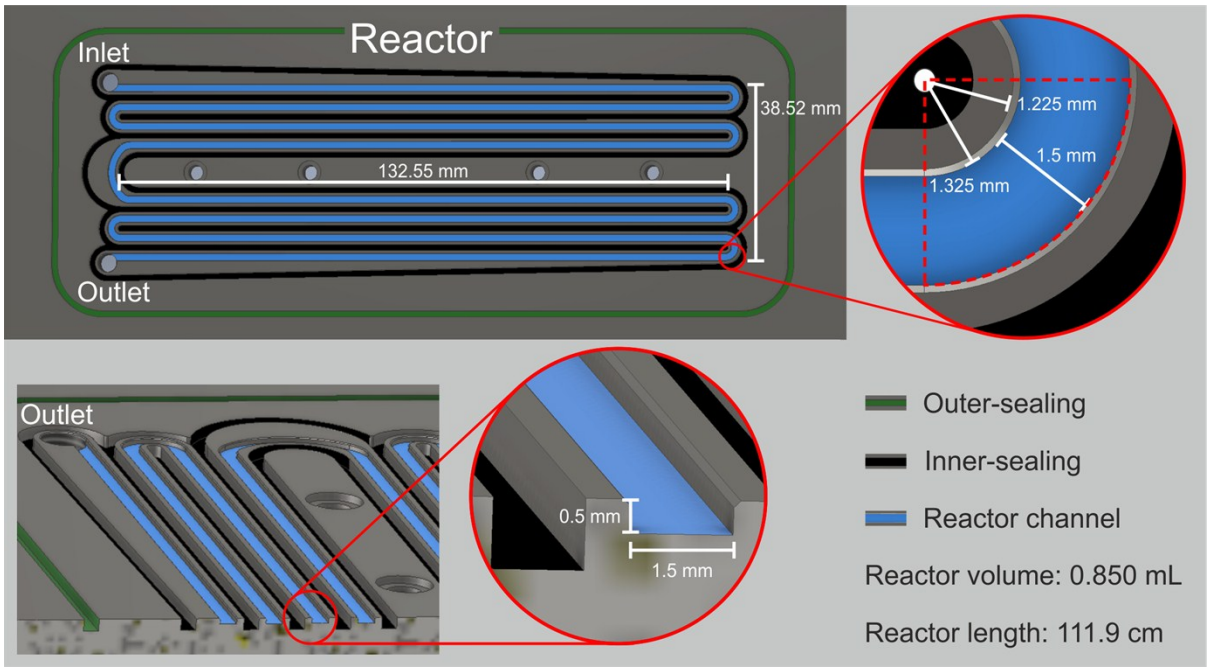

Figure S11. Technical drawing of the reactor plate.

The reactor volume was calculated by adding the irradiated volumes of the different geometrical elements, resulting in a volume of 0.85 mL. A photograph of the reactor plate with the milled channels colored according to Figure S11 is shown in Figure S12 together with a top view onto the closed reactor.

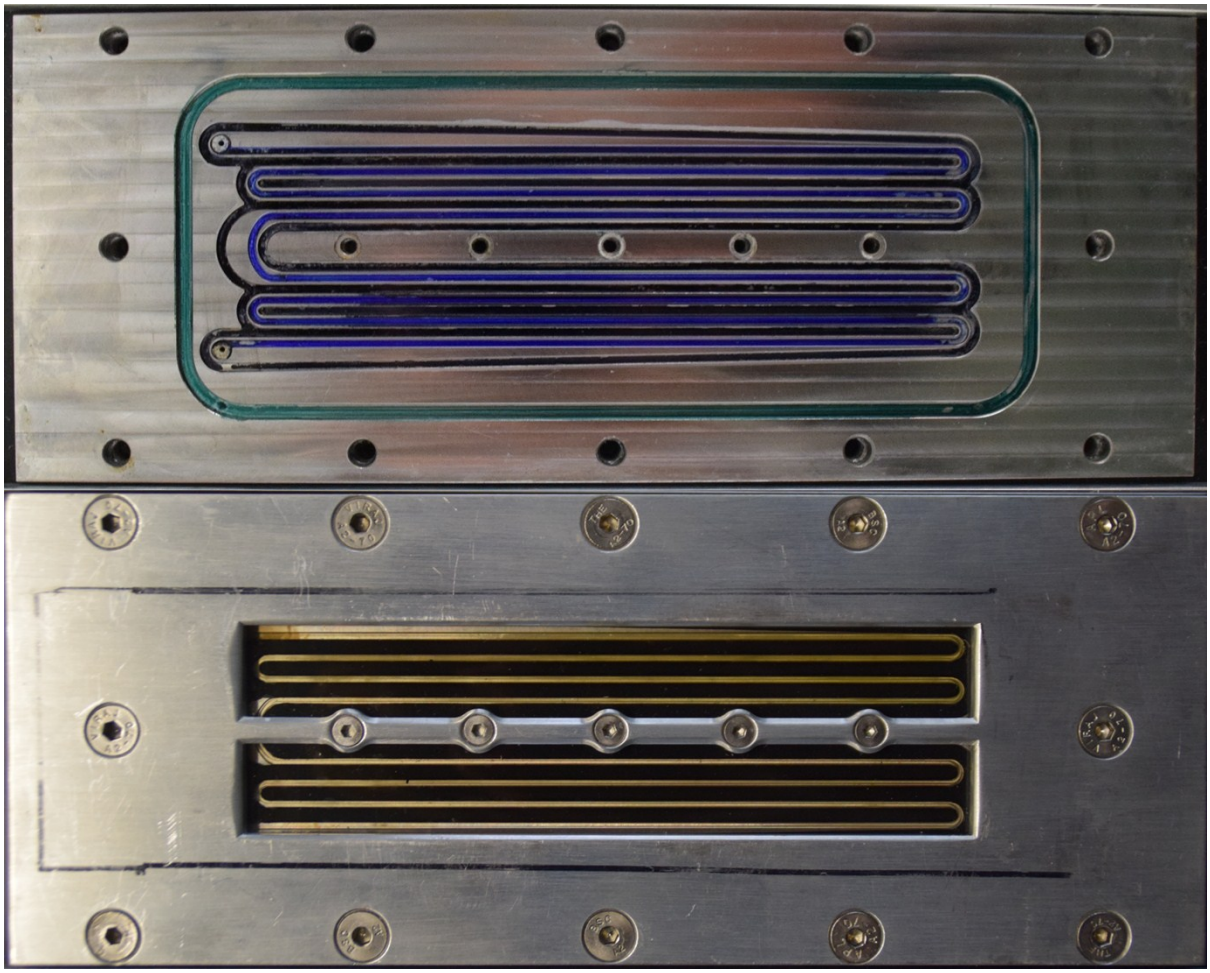

Figure S12. Top: Photograph of the reactor plate. Milled channels are colored according to Figure S11. Bottom: On top view onto the closed reactor.

The housing for the LED arrays was designed based on the reactor window. The electrical connectors were developed in a plug-and-play style so that the arrays could easily be exchanged. Figure S13 shows two photographs of the setup, including the radial fans which directed the air streams on the front and the rear side of the arrays. Cooling of the LED arrays turned out to be crucial to minimize wavelength shifts of the LEDs due to overheating and to make the screening reproducible.

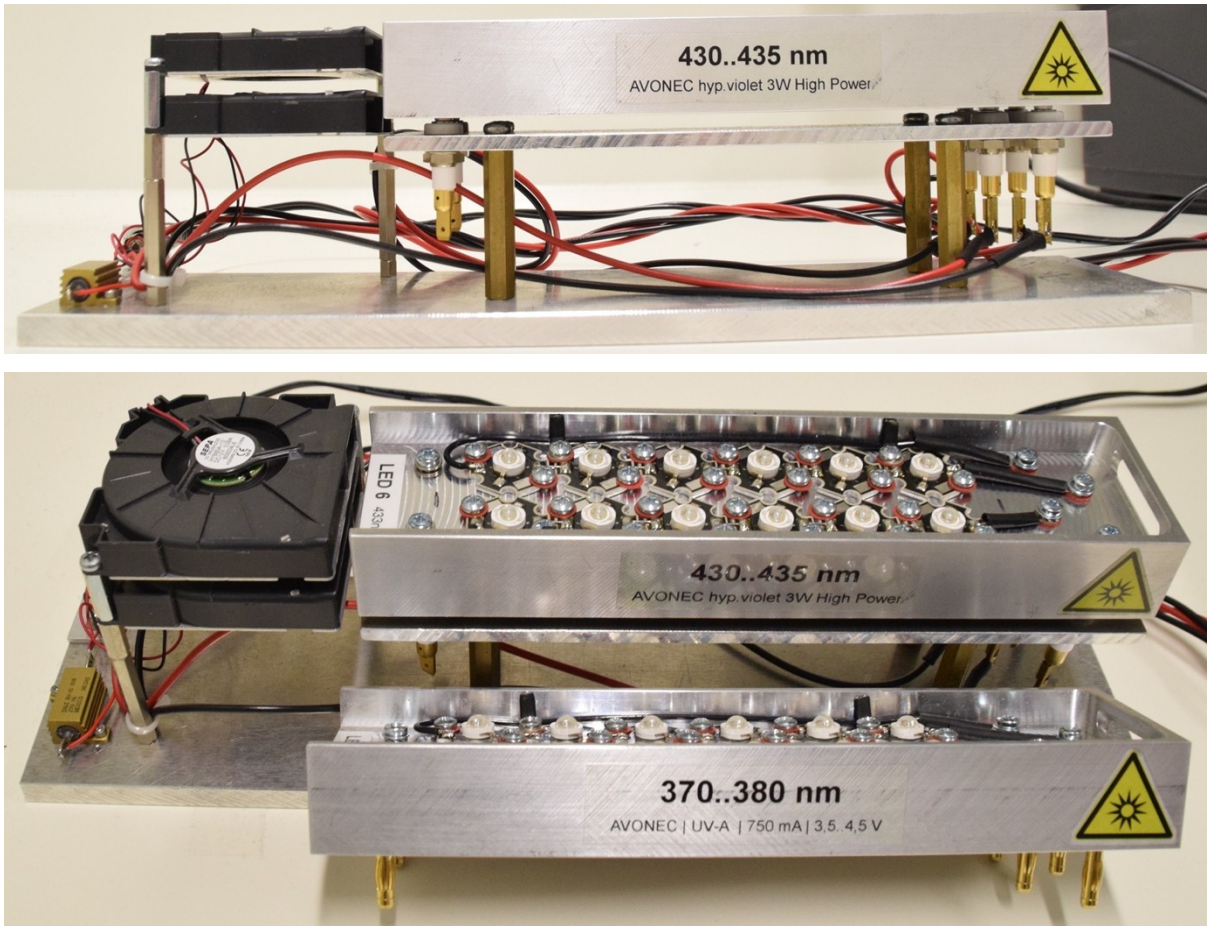

Figure S13. Photographs of the LED setup with radial fans fixed in front of the array.

S4) Irradiance-matching of the LED arrays

LED arrays were assembled for 16 different emission maxima λ aiming to cover most of the visible light spectrum. Each LED array consisted of twelve high-power LEDs of which six each were serially connected in two parallel strings connected to an adjustable power supply with two channels (35 V, 4 A, EX354RT, Aim-TTi, Huntingdon, UK). Table S2 summarizes information about the single LEDs.

Table S2. Employed LEDs which were assembled into LED arrays.

λ (nm)	Power[a] (W)	Product name	Vendor	Costs[b] (€)
370	5.00	Roschwege Star-UV365-05-00-00	Conrad[c]	104.00
373	3.00	3 W High Power LED 370nm–380nm	Avonec[d]	6.05
385	3.00	3 W High Power LED 380nm–390nm	Avonec	4.65
405	3.00	Roschwege Star-UV405-03-00-00	Conrad	18.73
416	3.00	3 W High Power LED 410nm–420nm	Avonec	2.40
429	3.00	3 W High Power LED 430nm–435nm	Avonec	1.85
444	2.17	ILH-OW01-DEBL-SC211-WIR200	RS Components[e]	7.45
463	2.17	ILH-OW01-BLUE-SC211-WIR200	RS Components	6.47
494	3.00	3 W High Power LED 490nm–495nm	Avonec	2.33
503	2.24	ILH-GD01-VEGR-SC201	RS Components	7.01
516	3.00	3 W High Power LED 515nm–525nm	Avonec	1.44
521	2.17	ILH-OW01-TRGR-SC211	RS Components	7.81
536	1.92	ILH-LC01-MINT-SC201-WIR200	RS Components	9.96
596	1.61	ILH-OW01-YELL-SC211-WIR200	RS Components	7.09
643	1.62	ILH-GD01-RED1-SC201	RS Components	4.78
668	1.62	ILH-GD01-HYRE-SC201	RS Components	7.88

[a] Maximal electrical power specified by the vendor. [b] Costs per LED. [c] Conrad Electronic SE (Hirschau, Germany). [d] Avonec (Essen, Germany). [e] RS Components (Corby, UK).

For the irradiance-matching of the 16 LED arrays, a calibrated spectroradiometer PS–200 (Apogee Instruments, Logan, UT) was acquired. Spectroradiometers are calibrated in a specified wavelength range to measure spectral output in absolute units like the photon flux density (in µmol m^{-2} s^{-1} nm^{-1}). Recorded emission spectra can be

integrated over a certain area of wavelengths to obtain a measure of the irradiance, i.e., the power spectral density (PSD, in µmol m^{-2} s^{-1}). For the matching of the irradiances, the PSDs of the LED arrays were calibrated as a function of the applied current adjusted by the power supply. To detect only the photons that pass the reactor window, the reactor plate was removed and the spectroradiometer was placed directly behind the FEP foil. As a first measurement, the area of the reactor window was segmented into squares with 8 mm edge length (according to the outer diameter of the spectroradiometer's detector) to investigate irradiation homogeneity. The window length (140 mm, x coordinate) was divided into 17 segments and the window width (40 mm, y coordinate) into 8 segments. Figure S14 illustrates the irradiation intensity profile over the reactor grid for the 596nm-array, highlighting intensity variations by a factor >2 over the reactor area.

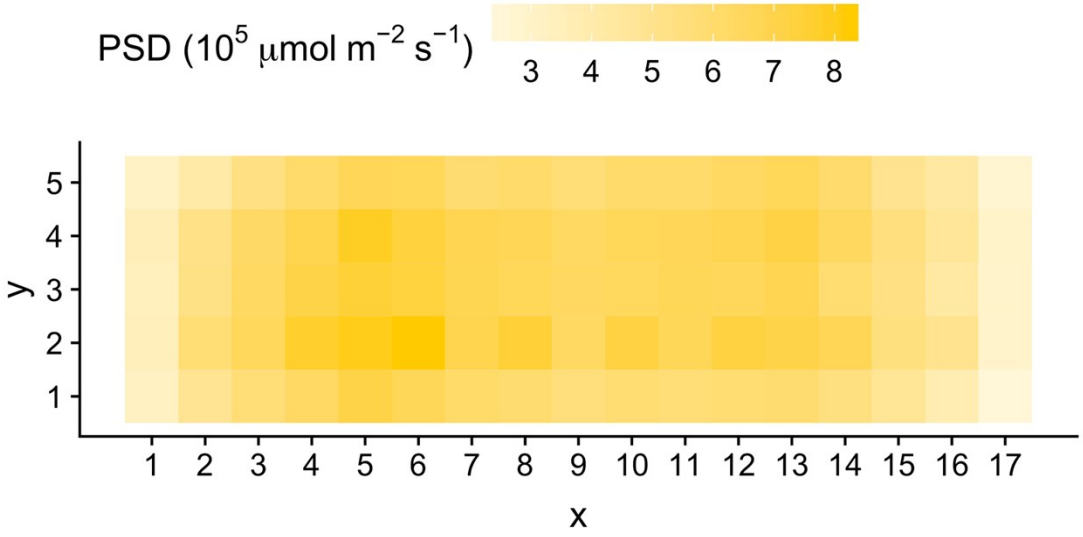

Figure S14. Irradiation intensity profile over the reactor area using the 596nm-array at a current of 700 mA.

Considering the nonuniform intensity profile, ten measurement points were distributed over the segmented grid. Moreover, ten control points were introduced where the matching of the LED arrays could be confirmed. Figure S15 shows the measurement and the control points on the reactor window grid.

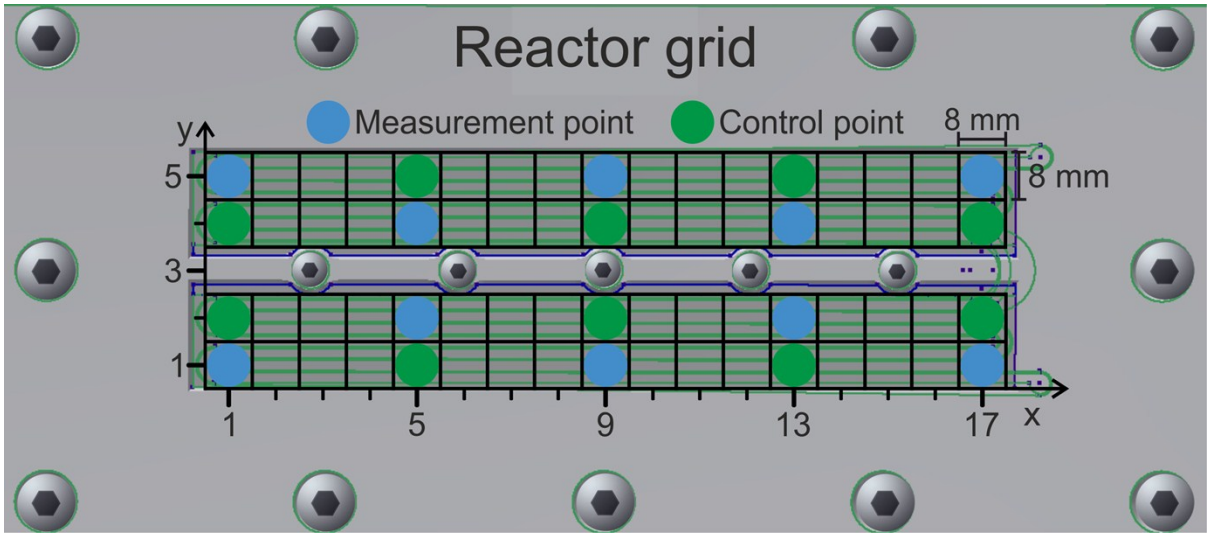

Figure S15. Position of the measurement and control points on the reactor grid for the matching of the LED arrays.

To gate the measurement and control points precisely and highly reproducible with the spectroradiometer, scaffolds were 3D-printed using an Ultimaker 2+ (Ultimaker, Utrecht, The Netherlands). Figure S16 shows the scaffold for the measurement points and for the control points considering that the detector itself had an outer diameter of 31.5 mm while the light collecting area only had a diameter of 8 mm.

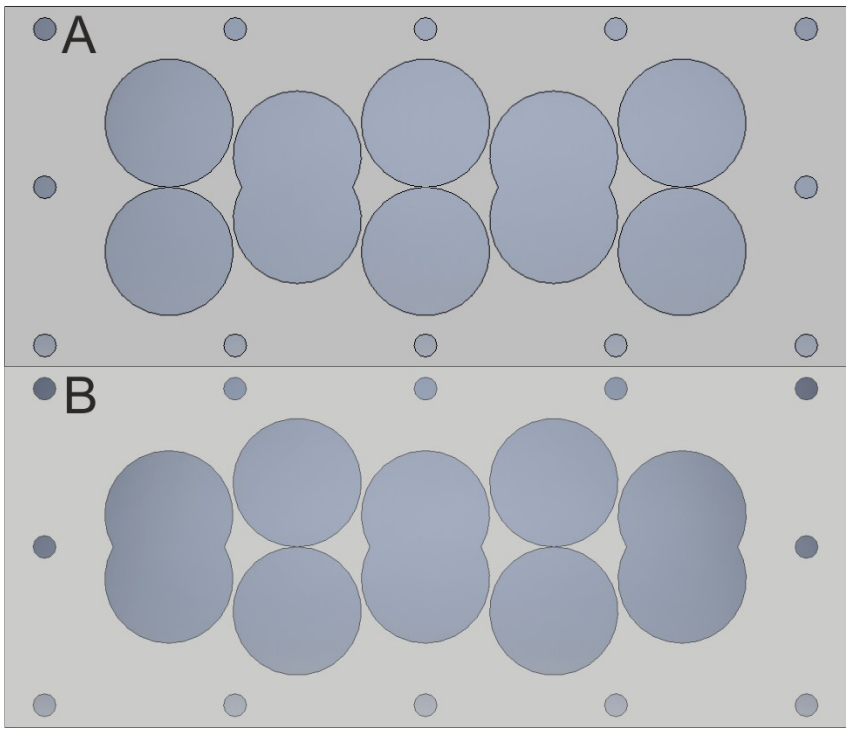

Figure S16. Scaffolds to precisely locate the measurements of irradiances. A: Measurement points. B: Control points.

The scaffolds could be screwed directly onto the FEP foil and the detector of the spectroradiometer fitted exactly to the holes. Figure S17 shows a photograph of the final matching setup.

Figure S17. Photograph of the final matching setup with the spectroradiometer fixed directly on the FEP foil and positioned by the 3D-printed scaffold.

To match the LED arrays conveniently to any desired irradiance, the PSD of the arrays was calibrated as a function of the applied current. Therefore, the PSDs of all ten measurement points were added and the summed PSD value was plotted against the applied current. As an example, Figure S18B illustrates the calibration curve for the 569nm-array, fitted by a fifth-grade polynomial. The normalized emission spectrum of the array is shown in Figure S18A.

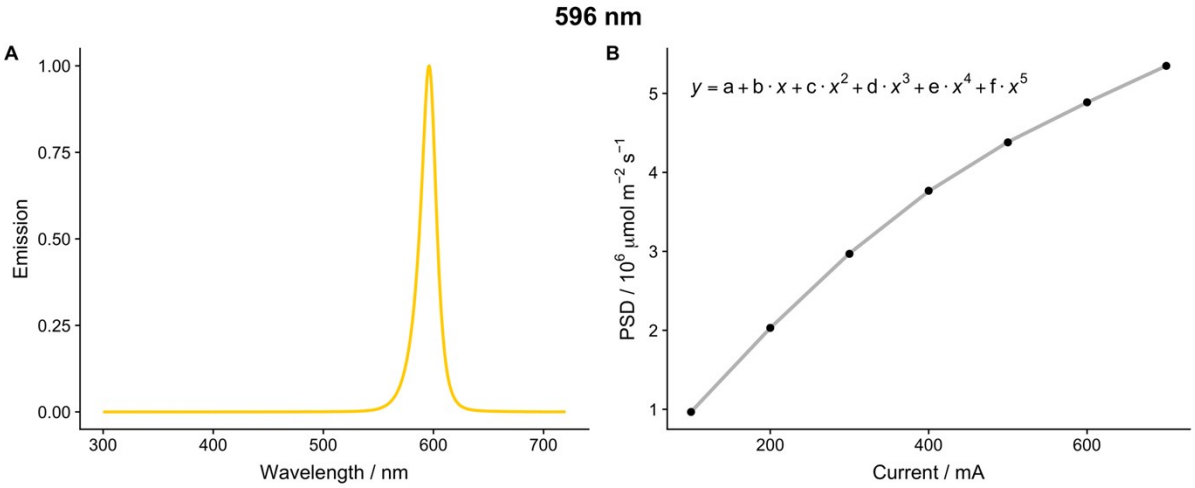

Figure S18. A: Normalized emission spectrum of the 596nm-array; B: Calibration curve for the sum of the ten PSDs recorded at the measurement points as a function of the applied current.

This calibration procedure was carried out for all LED arrays with an emission maximum >400 nm. Of these 13 LED arrays, the 596nm-array exhibited the lowest irradiance at maximum current (700 mA). Thus, the other 12 LED arrays were matched to the maximum PSD value of this array. The currents *I* needed to match the irradiance of the arrays could be conveniently calculated from the calibration curves. To validate this approach of matching, the irradiances at the control points of all LED arrays with the matching current *I* applied were measured and compared to the 596nm-array. The deviations are summarized in Table S3. With a maximum deviation of only 2% in the summed PSD values, the accuracy of the method was verified to prove that all LED arrays irradiate almost the same amount of photons per time on the reactor area.

Table S3. Deviations of the summed PSDs of the control points compared to the 596nm-array.

λ (nm)	I (mA)	Deviation (%)
405	277	2
416	216	2
429	182	< 1
444	177	1
463	185	< 1
494	137	1
503	174	< 1
516	159	1
521	174	< 1
536	168	2
596	700	—
643	249	< 1
668	328	< 1

Due to the observation of another wavelength-selective reaction channel at wavelengths <450 nm (see main text, Figure 2), we decided to acquire three more LED arrays with emission maxima <400 nm. However, the combination of the PMMA plate and the FEP foil used as a pane for the window (Figure S8) exhibited significantly decreasing transmissions for light near the UV-A spectrum (Figure S9). Since the high irradiances of the high-power LEDs provided the advantages of very short reaction times and high process efficiencies, we decided to not push down the irradiance of all LED arrays by a factor ~3 but instead perform a new matching. The procedure of the calibration process was adapted from the one described above. The three LED arrays were matched to the irradiance of the 373nm-array, which showed the lowest irradiance at maximum current. This value was only ~30% of the matched irradiance above. Therefore, also the 405 nm array was matched to this lower intensity and the reaction time was adjusted such that the reaction with the 405nm-array showed the same conversion and yield as above (7.1 min reaction time instead of 1.7 min above). For the screenings in the main text (Figure 2) the prolonged reaction times were used

for the three LED arrays with emission maxima <400 nm. Table S4 summarizes the deviation of the matching recorded on the control points.

Table S4. Deviations of the summed PSDs of the control points compared to the 373nm-array.

λ (nm)	I (mA)	Deviation (%)
370	385	1
373	700	—
382	461	< 3
405	82	< 2

S5) Reaction time screening

As described in the main text, the work of Noël and co-workers was reproduced using DBU instead of TMEDA as an amine base (Scheme 1a, main text).[S2] Due to the here employed high irradiance of the 521nm-array, which irradiates directly into the absorption band of eosin Y, the catalyst loading could be reduced to 2 mol%. With this catalyst loading, the reaction provides reasonable conversions in short reaction times. Figure S19 illustrates the results of the reaction time screening, which decided over the reaction conditions for the subsequent wavelength screenings.

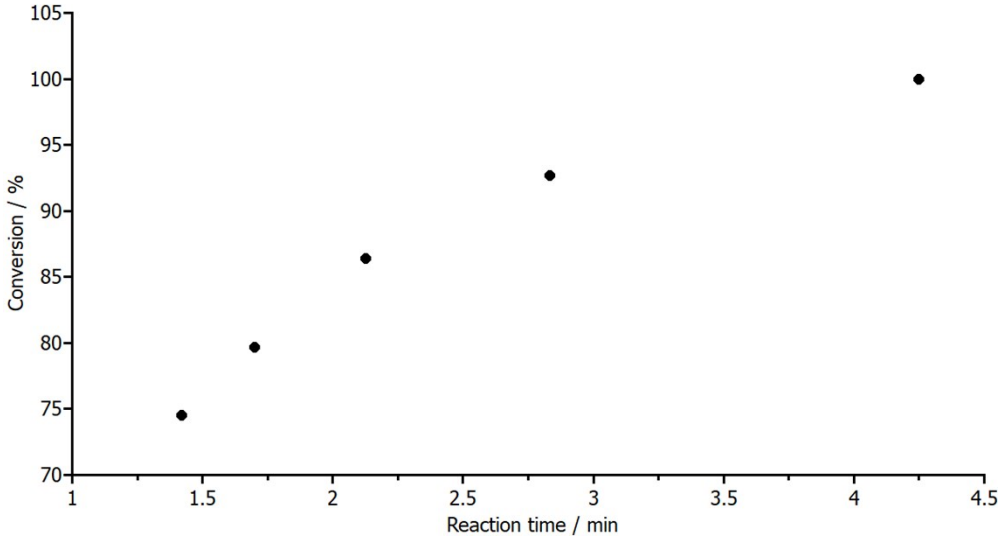

Figure S19. Reaction time screening under the following reaction conditions: $[\mathbf{1}]_0$ = 0.0175 mol L^{-1}, 2.0 equiv. **2**, 3.0 equiv. DBU, 2 mol% eosin Y, MeCN, ambient temperature, irradiance-matched 521nm-array.

During the reaction time (Figure S19) and wavelength screenings (Figure 2, main text), we observed an issue already described by Noël and co-workers, that is, the use of DBU led to black, non-transparent reaction solutions at long reaction times.[S2] This issue could be overcome by utilizing the reaction channel via the EDA complex between the substrates **1** and **2** which, however, came at the price of longer reaction times (Table 1, main text).

S6) Offline NMR analysis

Since it was not possible to separate the single regioisomers **3** and **4** from each other (neither by flash chromatography nor by preparative RP chromatography), a mixture of regioisomers was isolated. In this mixture, the molecular ion peak was found using mass spectrometry (HRMS, ESI$^+$, m/z calculated for $C_{13}H_7F_9N$ $[M]^+$: 348.0440; m/z found: 348.0443). Nuclear magnetic resonance (NMR) spectroscopy was used to determine the exact chemical structure of the substances. Besides one-dimensional NMR experiments (^{1}H, ^{13}C, ^{19}F), the two-dimensional NMR experiments DQF-COSY, HSQC, and HMBC were used for structural elucidation. Due to the two signal sets visible in the spectra, all meaningful signals were assigned by their according atom number (Scheme S2).

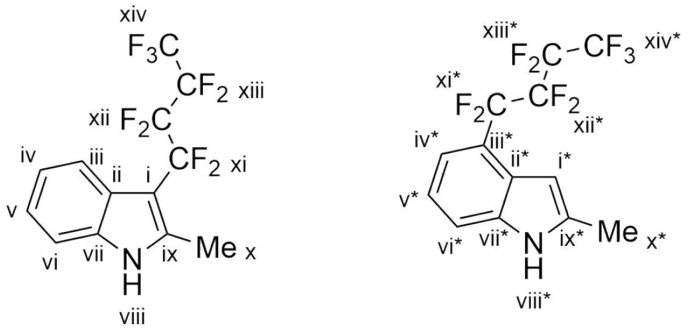

3 **4**

Scheme S2. Regioisomeric perfluoroalkylated indoles **3** and **4** with enumberated atoms. The positions in the minor product **4** are marked with an asterisk.

The NMR signals of the main product **3** were found to be in good agreement with the previous report.[S2] All signals were assigned according to Scheme S2.

1-methyl-3-(perfluorobutyl)-1*H*-indole (**3**):

^{1}H NMR (500 MHz, DMSO-d$_6$) δ = 11.87 (s, 1H, H_{viii}), 7.45 (d, J = 7.9 Hz, 1H, H_{iii}), 7.42–7.38 (m, 1H, H_{vi}), 7.17–7.13 (m, 1H, H_v), 7.11–7.06 (m, 1H, H_{iv}), 2.47 (m, 3H, H_x).

^{13}C NMR (125 MHz, DMSO-d$_6$) δ = 138.8 (t, J = 4.9 Hz, C_{ix}), 134.8 (s, C_{vii}), 125.6 (t, J = 3.5 Hz, C_{ii}), 121.7 (s, C_v), 120.7 (s, C_{iv}), 118.1 (s, C_{iii}), 111.5 (s, C_{vi}), 97.5 (t, J = 27.3 Hz, C_i), 12.3 (s, C_x).

^{19}F NMR (282 MHz, DMSO-d_6) δ = −82.6 (m, 3F, F_{xiv}), −105.3 (m, 2F, F_{xi}), −124.8 (m, 2F, F_{xii}), −127.6 (m, 2F, F_{xiii}).

1-methyl-4-(perfluorobutyl)-1*H*-indole (**4**):

^{1}H NMR (500 MHz, DMSO-d_6) δ = 11.44 (s, 1H, H_{viii*}), 7.57 (d, *J* = 7.8 Hz, 1H, H_{vi*}), 7.23–7.17 (m, 2H, H_{iv*}, H_{v*}), 6.22 (s, 1H, H_{i*}), 2.42 (s, 3H, H_{x*}).

^{13}C NMR (125 MHz, DMSO-d_6) δ = 138.6 (s, C_{ix*}), 136.7 (s, C_{vii*}), 125.8 (t, *J* = 3.4 Hz, C_{ii*}), 119.4 (s, C_{v*}), 118.1 (s, C_{iv*}), 116.6 (C_{iii*}, from HMBC), 114.9 (s, C_{vi*}), 98.3 (s, C_{i*}), 13.2 (s, C_{x*}).

^{19}F NMR (282 MHz, DMSO-d_6) δ = −82.6 (m, 3F, F_{xiv*}), −110.0 (m, 2F, F_{xi*}), −124.2* (m, 2F, F_{xii*}), −127.4* (m, 2F, F_{xiii*}).

C_{iii*} of the minor product **4** could not be found in the ^{13}C NMR spectrum, which is due to the low sensitivity of the method combined with the ^{2}J coupling to the fluorine atoms splitting the signal into a triplet. However, a HMBC cross peak to H_{v*} could be found to assign a chemical shift to the signal. In the NMR spectra, moreover, traces of another regioisomer could be found. The signal intensities, though, were too low to elucidate its structure. The NMR spectra with assigned signals are attached. Thereafter, the ^{19}F-NMR experiments are presented which were used to characterize the EDA complexes.

^{1}H NMR

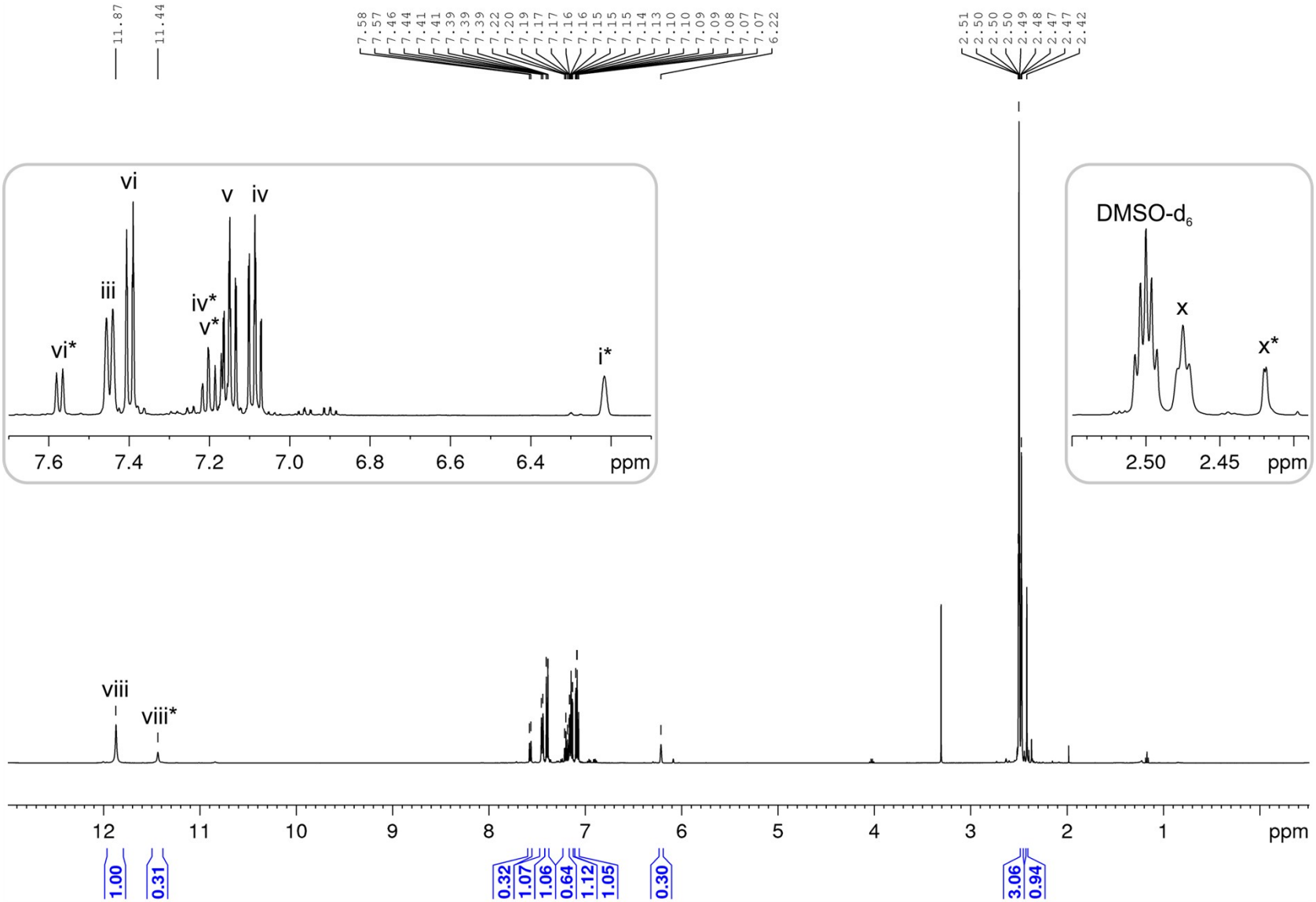
11.87
11.44
7.58
7.57
7.46
7.44
7.41
7.41
7.39
7.39
7.39
7.22
7.20
7.19
7.17
7.17
7.16
7.16
7.15
7.15
7.15
7.14
7.13
7.10
7.10
7.09
7.09
7.08
7.07
7.07
6.22
2.51
2.50
2.50
2.50
2.49
2.48
2.47
2.47
2.42
vi
v
iv
iii
iv*
v*
vi*
i*
7.6
7.4
7.2
7.0
6.8
6.6
6.4
ppm
DMSO-d6
x
x*
2.50
2.45
ppm
viii
viii*
12
11
10
9
8
7
6
5
4
3
2
1
ppm
1.00
0.31
0.32
1.07
1.06
0.64
1.12
1.05
0.30
3.06
0.94

^{13}C NMR

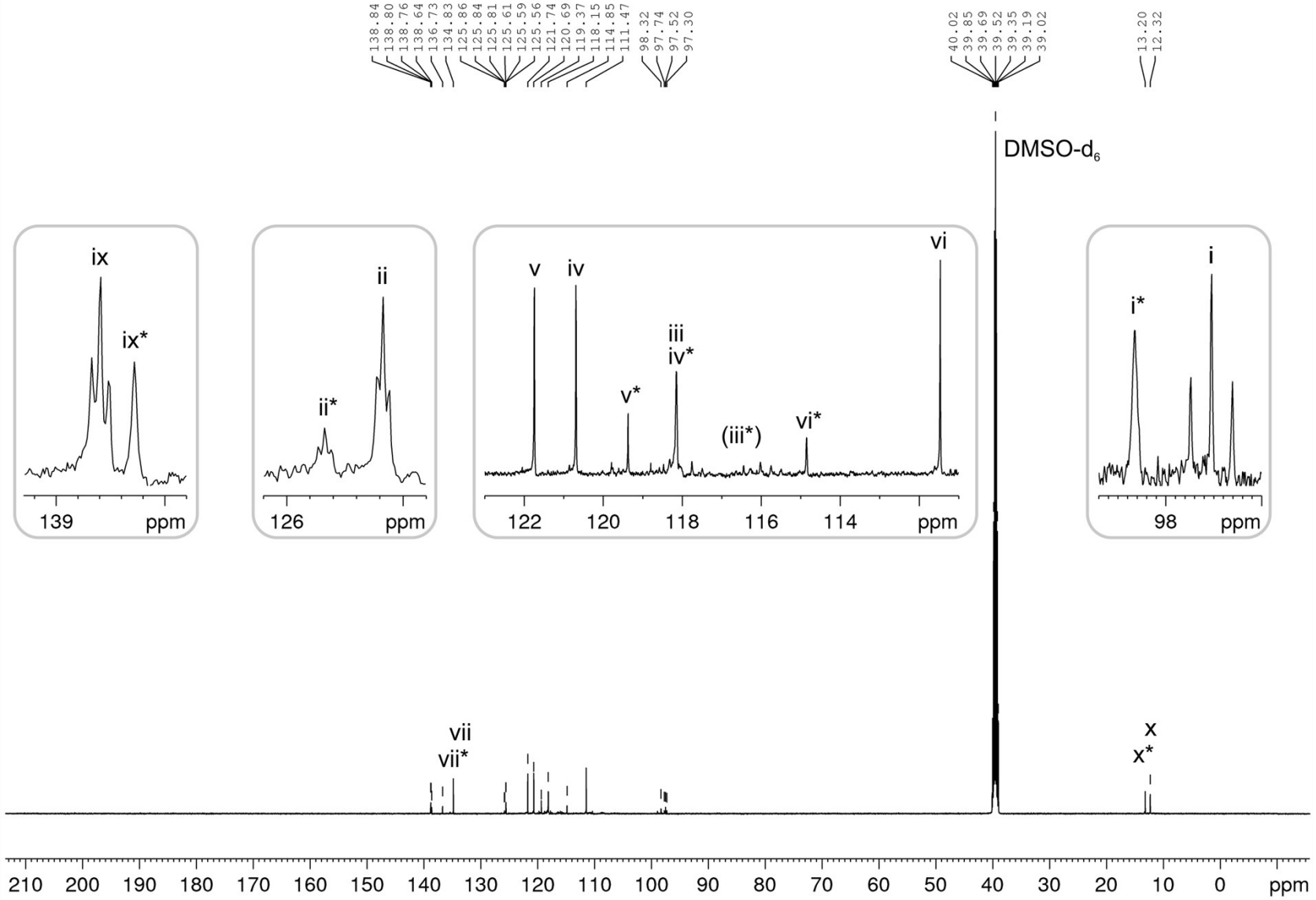
138.84
138.80
138.76
138.64
136.73
134.83
125.86
125.84
125.81
125.61
125.59
125.56
121.74
120.69
119.37
118.15
114.85
111.47
98.32
97.74
97.52
97.30
40.02
39.85
39.69
39.52
39.35
39.19
39.02
13.20
12.32
DMSO-d6
ix
ix*
ii
ii*
v
iv
v*
iii
iv*
(iii*)
vi*
vi
i
i*
vii
vii*
x
x*
139
ppm
126
ppm
122
120
118
116
114
ppm
98
ppm
210
200
190
180
170
160
150
140
130
120
110
100
90
80
70
60
50
40
30
20
10
0
ppm

^{19}F NMR

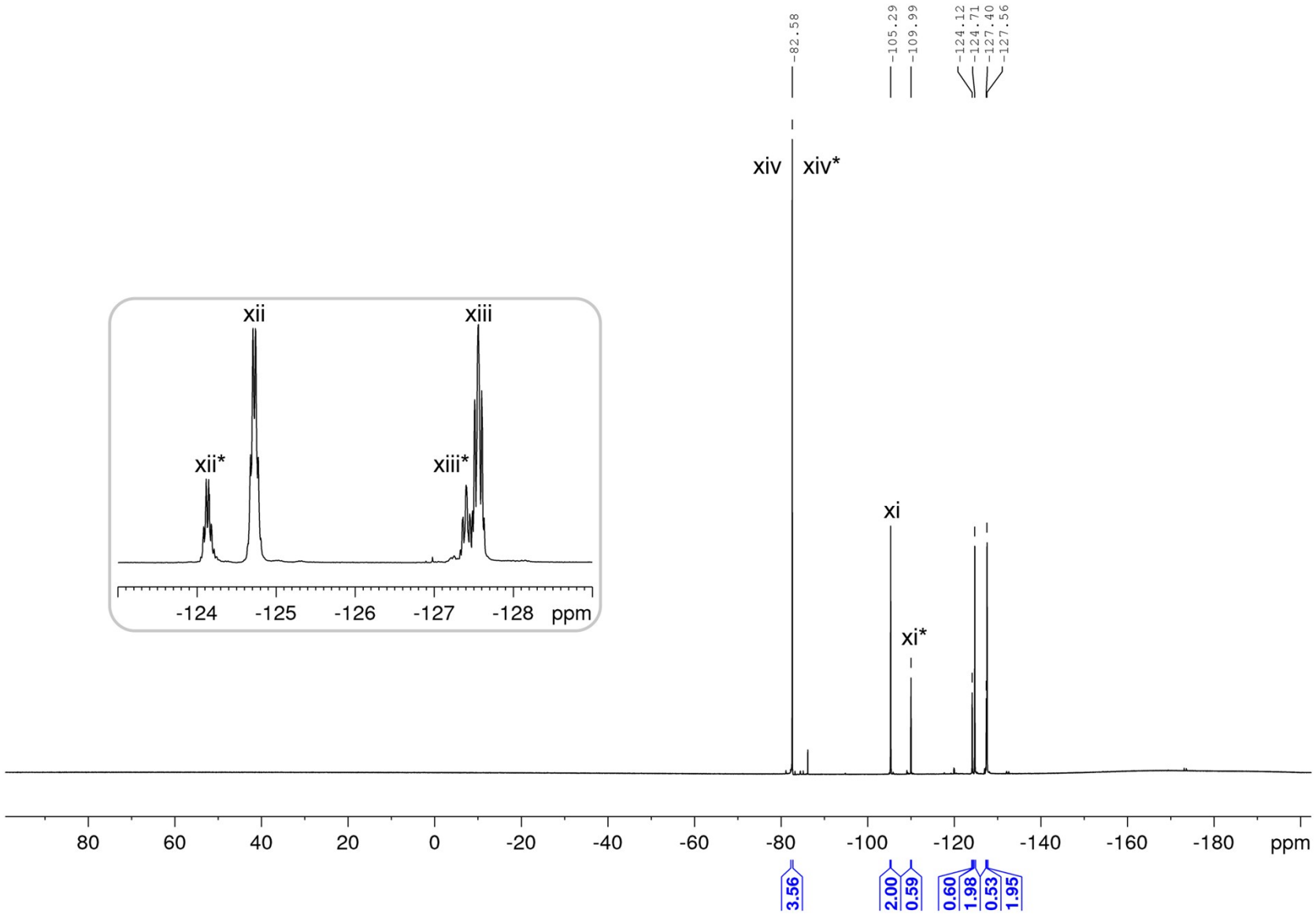
-82.58
-105.29
-109.99
-124.12
-124.71
-127.40
-127.56
xiv
xiv*
xi
xi*
xii
xii*
xiii
xiii*
-124
-125
-126
-127
-128
ppm
80
60
40
20
0
-20
-40
-60
-80
-100
-120
-140
-160
-180
ppm
3.56
2.00
0.59
0.60
1.98
0.53
1.95

DQF-COSY

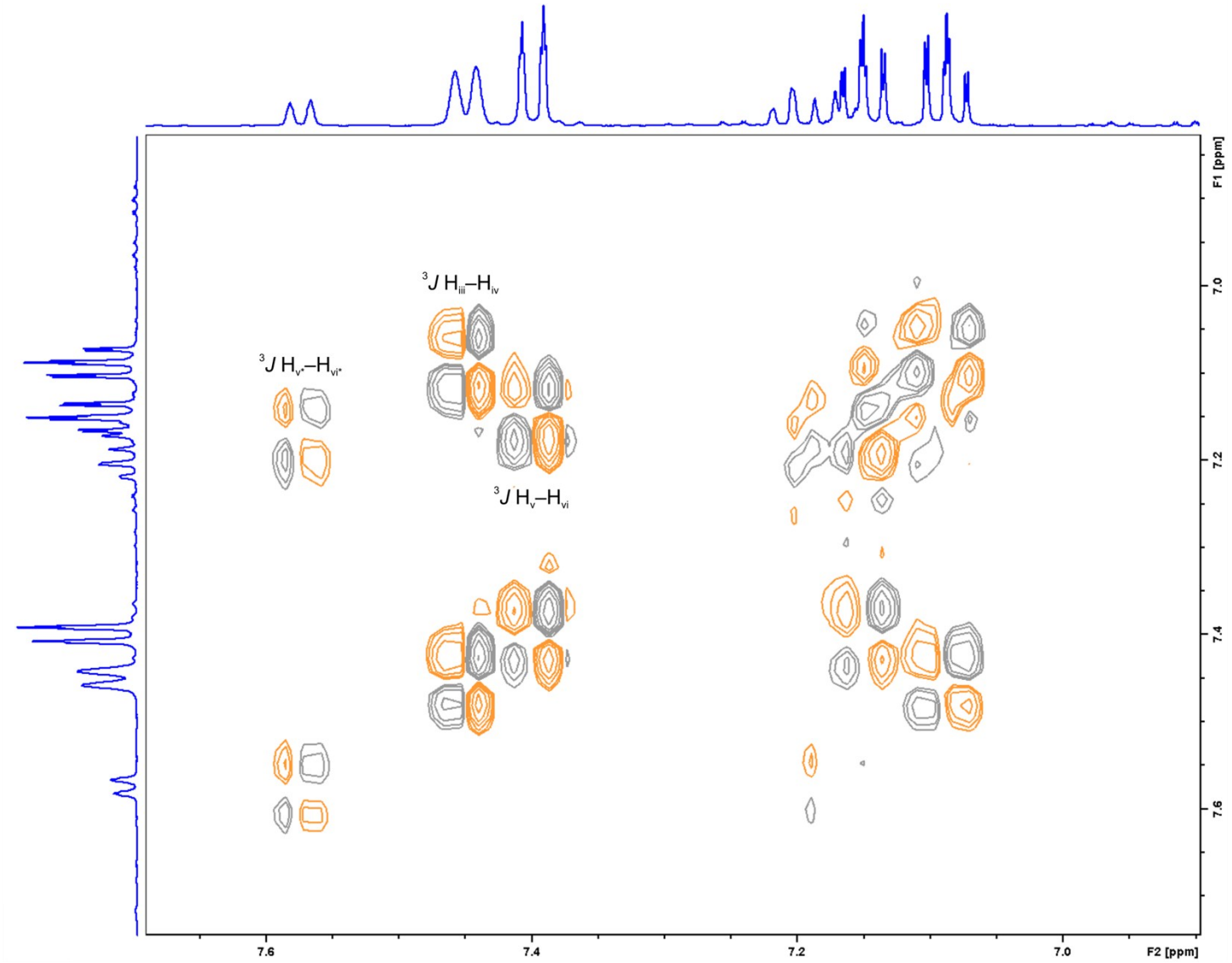

HSQC

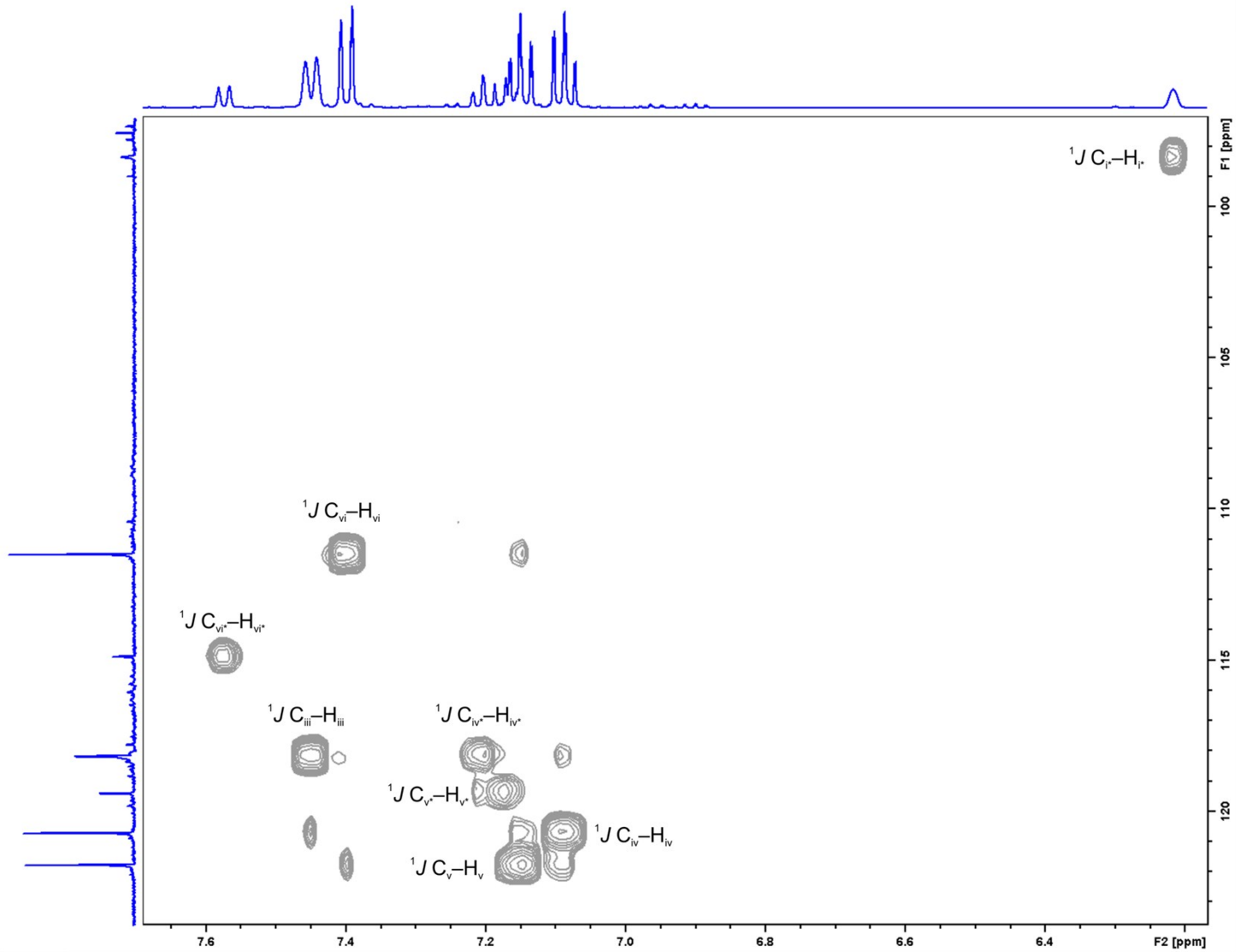
^1J C_{i*}–H_{i*}
^1J C_{vi}–H_{vi}
^1J C_{vi*}–H_{vi*}
^1J C_{iii}–H_{iii}
^1J C_{iv*}–H_{iv*}
^1J C_{v*}–H_{v*}
^1J C_{iv}–H_{iv}
^1J C_{v}–H_{v}
F1 [ppm]
100
105
110
115
120
7.6
7.4
7.2
7.0
6.8
6.6
6.4
F2 [ppm]

HMBC

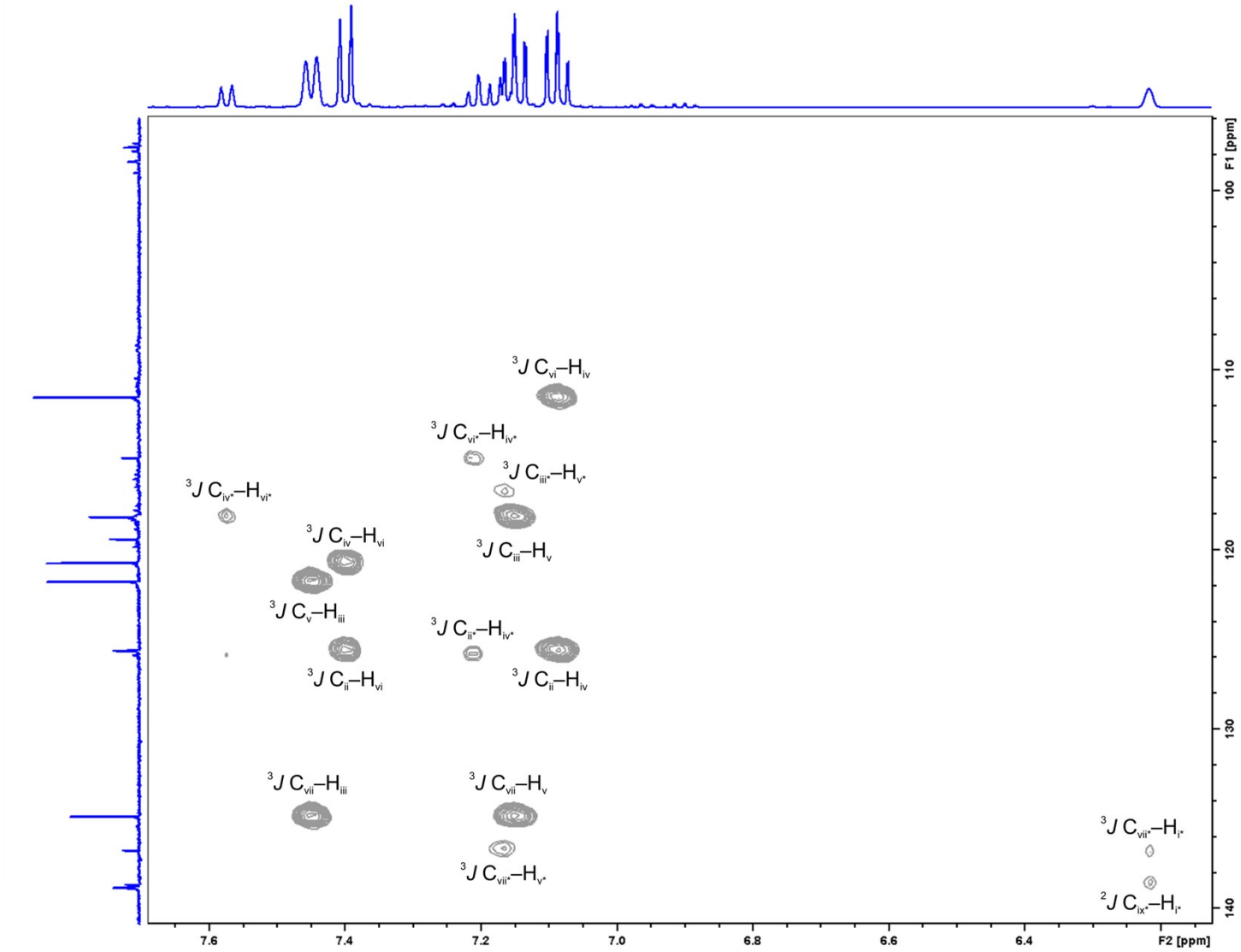
^{3}J C_{vi}–H_{iv}
^{3}J C_{vi*}–H_{iv*}
^{3}J C_{iii*}–H_{v*}
^{3}J C_{iv*}–H_{vi*}
^{3}J C_{iii}–H_{v}
^{3}J C_{iv}–H_{vi}
^{3}J C_{v}–H_{iii}
^{3}J C_{ii*}–H_{iv*}
^{3}J C_{ii}–H_{vi}
^{3}J C_{ii}–H_{iv}
^{3}J C_{vii}–H_{iii}
^{3}J C_{vii}–H_{v}
^{3}J C_{vii*}–H_{v*}
^{3}J C_{vii*}–H_{i*}
^{2}J C_{ix*}–H_{i*}
F1 [ppm]
100
110
120
130
140
7.6
7.4
7.2
7.0
6.8
6.6
6.4
F2 [ppm]

To characterize EDA complexes in this work, ^{19}F-NMR experiments were performed in the actual synthetic environment, i.e., with the given standard concentrations in acetonitrile. (Trifluoromethyl)benzene ($PhCF_3$) was added as internal standard. The results show that the displacement of the chemical shift of the CF_2-group next to the iodide (highlighted in blue) in the DBU-based EDA complex is much larger than the displacement for the indole-based EDA complex, which is only very small. If both electron donors (indole and DBU) are present in the solution, the displacement is similar to the DBU-based EDA complex, which means that primarily the DBU-EDA complex is formed in the reaction solution.

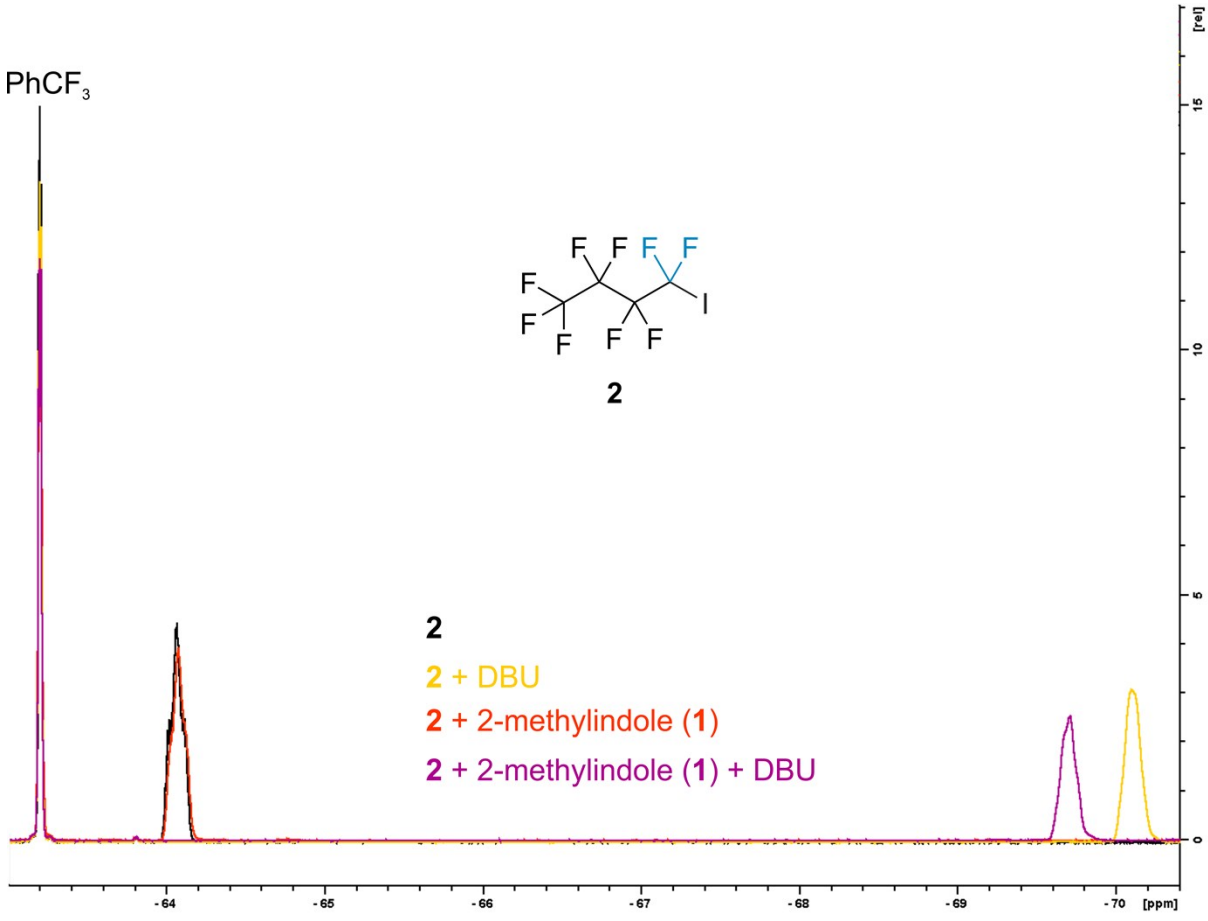

References

S1 C. P. Haas, T. Müllner, R. Kohns, D. Enke and U. Tallarek, *React. Chem. Eng.*, 2017, **2**, 498–511.

S2 N. Straathof, D. Osch, A. Schouten, X. Wang, J. Schouten, V. Hessel and T. Noël, *J. Flow Chem.*, 2014, **4**, 12–17.